Title

Crystallographic and electronic evolution of lanthanum strontium ferrite (La 0.6 Sr 0.4 FeO 3−δ) thin film and bulk model systems during iron exsolution

Journal

Physical Chemistry Chemical Physics, 21(7)

ISSN

0956-5000

Authors

Götsch, Thomas

Köpfle, Norbert

Grünbacher, Matthias

et al.

Publication Date

2019-02-13

DOI

10.1039/c8cp07743f

Peer reviewed

Crystallographic and electronic evolution of lanthanum strontium ferrite ($La_{0.6}Sr_{0.4}FeO_{3-\delta}$) thin film and bulk model systems during iron exsolution

Thomas Götsch, [abc] Norbert Köpfle,[a] Matthias Grünbacher,[a] Johannes Bernardi,[d] Emilia A. Carbonio, [ce] Michael Hävecker,[bc] Axel Knop-Gericke,[bc] Maged F. Bekheet, [f] Lukas Schlicker, [f] Andrew Doran, [g] Aleksander Gurlo, [f] Alexandra Franz,[h] Bernhard Klötzer[a] and Simon Penner *[a]

We study the changes in the crystallographic phases and in the chemical states during the iron exsolution process of lanthanum strontium ferrite (LSF, $La_{0.6}Sr_{0.4}FeO_{3-\delta}$). By using thin films of orthorhombic LSF, grown epitaxially on NaCl(001) and rhombohedral LSF powder, the materials gap is bridged. The orthorhombic material transforms into a fluorite structure after the exsolution has begun, which further hinders this process. For the powder material, by a combination of *in situ* core level spectroscopy and *ex situ* neutron diffraction, we could directly highlight differences in the Fe chemical nature between surface and bulk: whereas the bulk contains Fe(IV) in the fully oxidized state, the surface spectra can be described perfectly by the sole presence of Fe(III). We also present corresponding magnetic and oxygen vacancy concentration data of reduced rhombohedral LSF that did not undergo a phase transformation to the cubic perovskite system based on neutron diffraction data.

1 Introduction

Recently, reduction-invoked exsolution processes have gained interest as pathways to create supported metal-oxide systems from complex materials such as perovskite oxides *in situ*.[1] During exsolution, one of the constituent ions of the oxide leaves its lattice site(s) and accumulates on the surface, *e.g.* in the form of metallic nanoparticles.[1–3] While these phenomena might be undesired in a lot of cases as it can lead to mechanical instabilities in a variety of applications, the resulting supported systems are of special interest for heterogeneous catalysis and electrocatalysis,[4] where the metal-oxide phase boundary plays a vital role. In order to better steer these processes and either prohibit them or potentially control the resulting morphologies and phase boundary sizes, a detailed understanding about the reaction steps at a fundamental level is required. This includes the effects of externally applied parameters like temperature or partial pressures,[2–7] as well as intrinsic properties of the materials like site deficiencies,[1] or phase transformations.[3,8,9]

One type of perovskite that has been shown to be suitable as a model system to study exsolution processes is lanthanum strontium ferrite (LSF), $La_xSr_{1-x}FeO_{3-\delta}$, which is a proposed anode material for solid oxide fuel cells, where it is exposed to reductive conditions. In previous studies, it was found that, upon reduction (either chemically or electrochemically), metallic iron particles are formed at the surface.[2–4] In this work, we investigate the exsolution from LSF with the composition $La_{0.6}Sr_{0.4}FeO_{3-\delta}$. For this stoichiometry, multiple polymorphs, including rhombohedral, orthorhombic, tetragonal and cubic, exist.[10–13] At room temperature and in its fully oxidized state, however, the rhombohedral structure is the stable one, which was previously shown to transform to the cubic one prior to the exsolution.[3] Thus, we selected two sample types, bulk powder and thin film (in the 20 nm scale), with two different crystal structures (rhombohedral for the bulk system and orthorhombic for the thin film) for this work. The stabilization of the orthorhombic

[a] *Department of Physical Chemistry, Universität Innsbruck, A-6020 Innsbruck, Austria. E-mail: simon.penner@uibk.ac.at*
[b] *Department of Heterogeneous Reactions, Max-Planck-Institute for Chemical Energy Conversion, Stiftstraße 34-36, 45470 Mülheim an der Ruhr, Germany*
[c] *Department of Inorganic Chemistry, Fritz-Haber Institute of the Max-Planck Society, Faradayweg 4-6, 14195 Berlin, Germany*
[d] *University Service Center for Transmission Electron Microscopy, TU Wien, A-1040 Vienna, Austria*
[e] *Helmholtz-Zentrum Berlin für Materialien und Energie, 12489 Berlin, Germany*
[f] *Fachgebiet Keramische Werkstoffe, Chair of Advanced Ceramic Materials, Institut für Werkstoffwissenschaften und -technologien, Technische Universität Berlin, 10623 Berlin, Germany*
[g] *Advanced Light Source, Lawrence Berkeley National Laboratory Berkeley, USA*
[h] *Abteilung Struktur und Dynamik von Energiematerialien, Helmholtz-Zentrum Berlin für Materialien und Energie, 14109 Berlin, Germany*

structure in the thin film was achieved by an epitaxial templating effect from the freshly cleaved NaCl(001) substrate.[14,15]

The unsupported thin film (obtained after dissolution of the substrate) was used for *in situ* transmission electron microscopy studies to reveal possible phase transitions upon heating in the reducing conditions of high vacuum and their correlation to the exsolution of metallic iron. Previous *ex situ* X-ray photoelectron spectroscopy (XPS) studies of the bulk system revealed the presence of the Fe(III)/Fe(II) redox couple at all stages of oxidation,[3] whereas Moessbauer spectroscopy suggests Fe(IV) in the fully oxidized state that is subsequently reduced to Fe(III).[16–20] To analyze this apparent discrepancy further, we combined surface-sensitive near-ambient pressure core level spectroscopy and bulk-sensitive (*ex situ*) neutron diffraction (yielding magnetic information in addition to data like oxygen occupancies) to elucidate potential changes of the electronic structure at the surface.

2 Experimental

2.1 Thin film preparation

For the LSF thin films, commercially available LSF powder (Sigma Aldrich) was used as the target material, which was pressed into a pellet onto a tantalum spiral (10 nm in diameter) at a force of 20 kN and was subsequently mounted in our self-built direct-current ion beam sputter source, as described in ref. 21–23 Thin film preparation has been carried out using a modular high-vacuum apparatus (with a base pressure of 6×10^{-7} mbar).[14] The deposition was carried out in an Ar background pressure of 8×10^{-5} mbar using Ar-ions of 2 keV. As substrates, NaCl(001) single crystals were employed, which were heated to 573 K. The resulting films were subsequently floated off the substrate in distilled water and collected using TEM grids.

2.2 (*In situ*) electron microscopy

For transmission electron microscopy (TEM) a ThermoFischer TECNAI F20 S-TWIN analytical (high-resolution) transmission electron microscope (200 kV), equipped with an Apollo XLTW SDD X-ray detector, was utilized. A Gatan double tilt heating holder, enabling experiments with very quick temperature changes (multiple hundred K s^{-1}) up to 1273 K, was used to detect any potential exsolution phenomena and phase transitions.

2.3 *In situ* X-ray spectroscopy

In situ X-ray photoelectron spectroscopy (XPS) and X-ray absorption spectroscopy (XAS) were conducted at the ISISS-PGM beamline at BESSY II.[24] A differentially pumped Specs Phoibos 150 NAP with a 1 mm entrance aperture was used as the electron analyzer.[25] For these studies, small pellets (d = 10 mm) of the powder were formed using a hydraulic press. The experiments were conducted in gas atmospheres of 0.3 hPa, and the samples were heated using an infrared heater aimed at the backside of the sample plate (the temperature was measured both by a thermocouple as well as a pyrometer).

The XP spectra presented in this work are all corrected for the different beam intensities at different energies, as well as for the ionization cross sections and the asymmetry,[26,27] in order to make comparisons between different spectra, especially in the case of the depth profiles, easier to visualize. In order to determine the oxidation states in the Fe 2p region, separately recorded reference spectra of Fe_2O_3 and FeO (formed *in situ* by thermal decomposition of iron(II)oxalate) were used for the fitting procedures.[3,28] For the metallic species, on the other hand, an asymmetric peak shape was employed.

All X-ray absorption near edge structure (XANES) spectra were recorded in both, Auger electron yield (AEY) and total electron yield (TEY) modes. The spectral intensities were normalized with respect to the step-like background across the ionization edge.

2.4 X-ray and neutron diffraction

The powder samples used for the *ex situ* synchrotron X-ray and neutron diffraction experiments were heat-treated in a Schlenk tube in different atmospheres and at different temperatures. These conditions included air at 1173 K, nitrogen at 1173 K, as well as diluted hydrogen (5% in Ar) at 973 K. In all cases, heating and cooling rates were set to 100 K h^{-1}, while the target temperature was kept for 5 h. These settings were chosen in order to potentially inhibit the previously found phase transformation to the (metastable) cubic polymorph.[3] The gas flow was further set to 1 mL s^{-1}.

Neutron diffraction data were collected at the fine resolution diffractometer E9 (FIREPOD) installed at the BERII research reactor at the Helmholtz-Zentrum Berlin (Germany).[29] A Ge monochromator, plane (511), was used for the non-polarized neutron beam with a wavelength of 1.7982 Å. About 1 g of the respective samples were encapsulated in a 6 mm vanadium container.

Rietveld refinement of the neutron diffraction data was performed using the FULLPROF program.[30] The profile function 7 (Thompson–Cox–Hastings pseudo-Voigt convoluted with an axial divergence asymmetry function) was used in all refinements.[31] In order to refine the magnetic structure, the magnetic irreducible representations for Fe at 6b site with propagation vector k = (0,0,0) were determined using the BASIREPS program software packages.[32]

High resolution synchrotron XRD patterns of the differently treated samples (see above) were acquired at beamline 12.2.2, Advanced Light Source at the Lawrence Berkeley National Labs (California, USA). The patterns were measured with the sample powder was placed in 0.7 mm capillaries in the angle-dispersive transmission mode with focused 25 keV monochromatic beam (λ = 0.4959 Å/30 μm spot size). Diffraction patterns were recorded using an RDI flat panel detector with dark image and strain correction. A NIST 660b LaB_6 standard was used to calibrate the measurement.[33,34]

3 Results and discussion

The two starting structures used in this work are displayed in Fig. 1. In Fig. 1A, the orthorhombic unit cell (space group no. 51, *Pmma*),[36] as observed for the sputter-deposited thin films,[35] is presented. The iron ions are coordinated by six oxygen atoms,

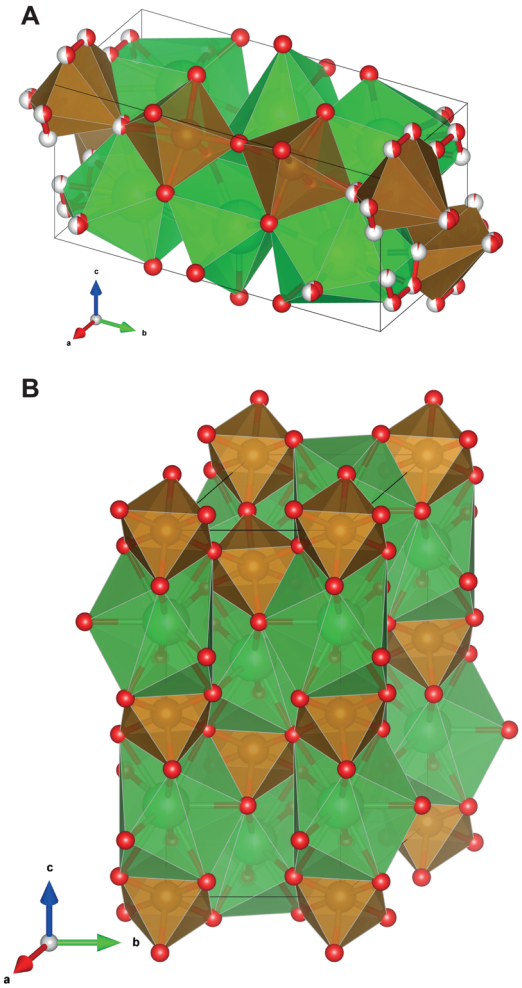

Fig. 1 LSF starting structures found for (A) the thin film,[35,36] and (B) the bulk sample.[3,12] The A site (La, Sr) is colored in green and the B site (Fe) in brown. Oxygen atoms are red.

forming chains of corner-shared distorted octahedra. Close to the (010) unit cell boundaries, there is a certain degree of disorder in the oxygen sites, leading to two distinct rotational configurations of the [FeO_6] octahedra.

The structure of the powder samples, which crystallize in space group no. 167 ($R\bar{3}c$), is rendered in Fig. 1B. This structure comprises a layer-like arrangement of corner-sharing [FeO_6] octahedra and edge-sharing [$(La,Sr)O_9$] polyhedra along the [001] direction. These layers are not fully two-dimensional, but rather form a three-dimensional network, with some of the lanthanum/strontium polyhedra intercalating between the iron-containing octahedra, and *vice versa*. Opposed to the structure of the thin film, there is no disorder within the unit cell, with each site featuring an occupancy of 1.

3.1 Orthorhombic LSF thin films

The LSF thin films deposited using our self-built sputter source were previously shown to be amorphous in their as-grown state,[35] crystallizing only upon further annealing. In this work, these amorphous sputter-deposited films were exposed to an *in situ* reduction program in the TEM (in high vacuum) using a heating holder.

Fig. 2A shows the selected area electron diffraction (SAED) patterns between 773 K and 923 K, where distinct differences can be observed. At 773 K, the diffraction pattern (displayed in the top left) contains features hinting at a starting crystallization process occurring in the initially amorphous thin film: the intensities of the diffraction rings are relatively low, and the rings appear to be very spotty and diffuse, suggesting a low degree of crystallinity. Upon increasing the temperature to 823 K (top right quadrant), the rings become more continuous and sharper. Additionally, the intensities increase, resulting in a better contrast in the pattern. When the film is further heated to 873 K (bottom right), the SAED pattern undergoes a drastic change, as seen by the altered relative intensities of the different rings. Since the rings that are present are more or less found at the same positions, this can, in principle, be explained by a rearrangement process or by a phase transformation. At higher temperatures, such as 923 K (lower left), the diffraction patterns do not exhibit any further significant changes. Some remnants of rings that started to vanish at 873 K are now completely gone, hinting at a single pure phase at this temperature.

In Fig. 2B, the azimuthally integrated intensity profiles (no background subtraction) of the SAED patterns between 773 K and 1173 K are displayed. These integrations were performed using the PASAD software.[37] The x-axis in this plot denotes the reciprocal distance, which corresponds to $1/d$ (with d being the respective lattice spacing). What could already be observed in panel A is discernible here, too: at the lowest temperature (bottom-most curve), the peak widths are large and the diffuse background is very pronounced, indicative of a weakly crystalline sample. By ramping up the temperature to 823 K, the peaks become much narrower and, as seen in the patterns in Fig. 2A, the relative intensities change – for instance, the peak at about 3.5 nm is now the most intense maximum. The phase transition can also be seen clearly: at 873 K, there is a change in the intensities, with the peak just below 3 nm^{-1} now being more intense than that at 3.5 nm^{-1}. The signal at 4.85 nm^{-1} is now visibly the strongest. Some of the peaks found in the previous pattern (at 823 K) are still visible as shoulders to the new intensities, for example at 3.5 nm^{-1} or 6.15 nm^{-1}. This suggests that, while the aforementioned phase transformation is in an advanced stage, it is not yet complete at the given temperature. These minor peaks, however, vanish completely at 923 K. At higher temperatures, the diffractogram does not exhibit any significant changes, with the peaks becoming a bit sharper, resulting in the apparent better separation of the small shoulder just below 6 nm^{-1}.

The first crystalline diffractogram, formed at a temperature of 823 K, can be assigned to an orthorhombic structure in the *Pmma* space group (see Fig. 1A).[36] This phase was previously observed for the same specimens after annealing the samples in air at 1073 K.[35] An overview of the assignment of the different lattice planes to the diffraction spots/rings of this pattern is given in the left half of Table 1. The inner-most ring, corresponding to a lattice spacing of 0.428 nm, can be assigned

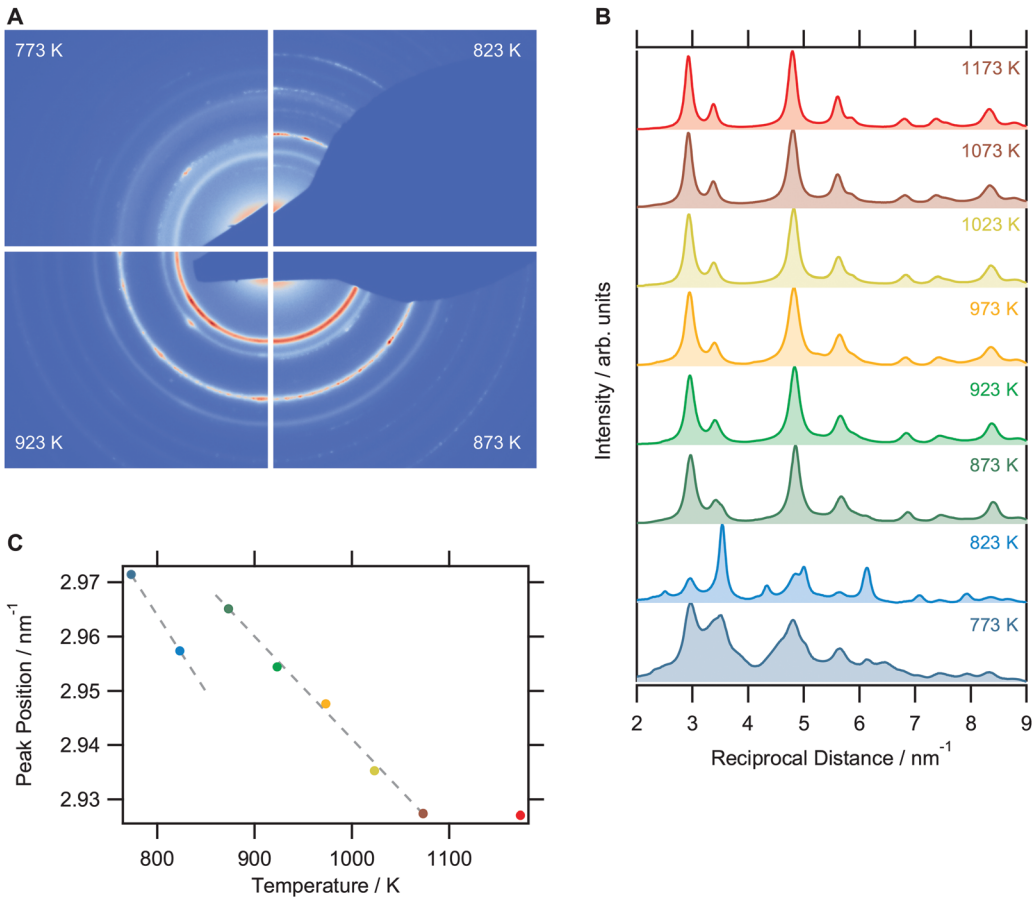

Fig. 2 (A) Comparison of SAED patterns at temperatures between 773 K and 923 K in high vacuum conditions. (B) Azimuthally integrated diffraction patterns, displayed as intensity profiles, for a temperature range of 773 K to 1173 K. (C) The position of the maximum just below 3 nm^{-1} (*Pmma* 031 and $Fm\bar{3}m$ 111, respectively) as a function of the temperature reveals a phase transformation between 823 K and 873 K, as seen from the dashed lines to guide the eye. The color code of the markers in (C) is the same as in panel (B).

Table 1 Assignment of the orthorhombic (*Pmma*) and cubic ($Fm\bar{3}m$) phases and their reflections (column "Refl.") to the diffraction patterns obtained at 823 K (after the first crystallization) and 923 K (after the phase transformation). *d* corresponds to measured spacings

823 K			923 K		
d/nm	Phase	Refl.	*d*/nm	Phase	Refl.
0.428	*Pmma*	(021)			
0.400	*Pmma*	(111)			
0.339	*Pmma*	(031)	0.337	$Fm\bar{3}m$	(111)
0.283	*Pmma*	(131)	0.292	$Fm\bar{3}m$	(200)
	Pmma	(200)			
0.231	*Pmma*	(221)			
0.207	*Pmma*	(240)	0.206	$Fm\bar{3}m$	(220)
	Fe $Im\bar{3}m$	(110)		Fe $Im\bar{3}m$	(110)
0.200	*Pmma*	(202)			
0.177	*Pmma*	(103)	0.176	$Fm\bar{3}m$	(311)
0.162	*Pmma*	(331)	0.169	$Fm\bar{3}m$	(222)
0.141	*Pmma*	(262)	0.146	$Fm\bar{3}m$	(400)
	Fe $Im\bar{3}m$	(200)		Fe $Im\bar{3}m$	(200)

to the (021) planes of the orthorhombic structure, whereas the signal at 0.400 nm stems from the (111) lattice planes of the orthorhombic system. Likewise, the peaks at 0.339 nm and 0.283 nm are ascribed to the (031) and (131/200) reflections, respectively.[36] At a lattice spacing of 0.207 nm, the ring does not only contain the *Pmma* (240) signals, but also those of metallic iron, crystallizing in a bcc lattice (space group no. 229, $Im\bar{3}m$),[38] the particles of which, formed *via* the exsolution process, are first found at this temperature (see the bright field TEM images below).

Since there is a lower number of spots in the diffraction pattern after the phase transition between 823 K and 873 K, this suggests a higher symmetry in the freshly formed phase. Unlike the powder system, which undergoes a phase transformation from the rhombohedral to the cubic perovskite structure that was stabilized by oxygen vacancies,[3] this new phase cannot be described by a cubic perovskite ($CaTiO_3$ type, space group no. 221, $Pm\bar{3}m$),[39,40] While all reflexes above 3.42 nm^{-1} (corresponding to lattice spacings of 0.292 nm and below) can be assigned to cubic perovskite spacings, the second-most intense peak of the diffractogram at d = 0.337 nm is not present in the $CaTiO_3$ structure.[39,40] In fact, this diffraction pattern cannot be attributed to any published LSF structure: neither to other orthorhombic lattices,[12,41] nor to tetragonal structures.[42] The rhombohedral phase that is the stable structure of the powder at room temperature (space group no. 167, $R\bar{3}c$) or another cubic phase (space group no. 227, $Fd\bar{3}m$) are not formed either.[12,43]

However, the rings in the diffraction pattern are characteristic for an fcc lattice (space group no. 225, $Fm\bar{3}m$) as it is, for example, found in the fluorite structure, *e.g.* in cubic zirconia or ceria,[44,45] or the NaCl type: the signal corresponding to 0.337 nm stems from the (111) planes, whereas the spacing of 0.292 nm can be ascribed to the (200) lattice planes. Likewise, the peak at 0.206 nm contains the $Fm\bar{3}m$ 220 reflex (in addition to the Fe (110) one), at 0.176 nm, the (311) rings are found and the (222) planes can be assigned to the spacing of 0.169 nm. A summary of this assignment is found in the right half of Table 1. It is, in principle, conceivable that the perovskite undergoes a potential decomposition into the pure oxides. However, La_2O_3 crystallizes in space group no. 229 ($Im\bar{3}m$),[46] and Fe_2O_3 in the Al_2O_3 type (space group no. 167, $R\bar{3}c$).[47] Similarly, Fe_3O_4 is a spinel (227, $Fd\bar{3}m$).[48] Only SrO and FeO crystallize in the NaCl structure type and, thus, in the correct space group (225, $Fm\bar{3}m$).[49,50] Nevertheless, the presence of these pure oxides can be excluded based on the fact that the lattice parameters do not match the diffraction pattern: for SrO, a = 5.16132 Å and the unit cell size of FeO is 4.3030 Å,[49,50] whereas the Rietveld analysis of the experimental pattern at 923 K (using EXPO2014[51]) yields a lattice parameter of 5.87 Å at the given temperature. This discrepancy could not be explained by thermal expansion alone as the linear coefficients of thermal expansion of SrO and FeO are 1.3716×10^{-5} K^{-1} and 1.34×10^{-5} K^{-1}, respectively,[52,53] yielding lattice parameters of 5.206 Å and 4.339 Å for SrO and FeO at 923 K. Thus, the only explanation for the presence of the $Fm\bar{3}m$ phase is the transformation of the perovskite into a solid solution that crystallizes in either the fluorite or the rock-salt type structure. Which of the two phases is formed is impossible to determine based on the SAED patterns alone – for this, much more complex techniques such as precession diffraction measurements would be required (as XRD does not yield sufficient signal intensities for these thin films).[54] However, an estimate can be given based on the degree of reduction of the perovskite since the formal sum formula of the fluorite would be AO_2 and that of the rock-salt structure AO (with A describing all the cations). Hence, the fluorite type should be preferred if the stoichiometric coefficient of oxygen is larger than one, and the rock-salt structure is expected for values of one and below (since it is easier for the structure to accommodate vacancies as opposed to an excess of anions).

In fact, a rough estimate of this oxygen deficiency can be made: under the assumption that, in the fully oxidized state, LSF ($La_{0.6}Sr_{0.4}FeO_{3-\delta}$) only contains Fe^{3+} species (as previously found using XPS),[3] the sum formula in that state can be written as $La_{0.6}Sr_{0.4}FeO_{2.8}$ when adhering to charge neutrality (*i.e.* the substitution of La^{3+} by Sr^{2+} ions leads to the formation of one oxygen vacancy per two Sr^{2+}). Since the transformation to the $Fm\bar{3}m$ lattice occurs under reducing conditions, the oxygen concentration is expected to be further diminished. The fluorite formula can generally be written so that all cations sum up to a stoichiometric coefficient of 1 (AO_{2-x}, with A being the sum of all cations in the structure and x the oxygen deficiency—x is used here to make the distinction from the δ of the perovskite more clear). In contrast, that of the perovskite contains two units of cations ($A_2O_{3-\delta}$); thus, the sum formula of the fully oxidized LSF species ($La_{0.6}Sr_{0.4}FeO_{2.8}$) can be rewritten in the fluorite scheme, yielding $La_{0.3}Sr_{0.2}Fe_{0.5}O_{1.4}$. The x is already very large in the oxidized state (x = 0.6), hinting at a severely reduced material with respect to the fluorite formula. Thus, due to the additional reduction occurring prior to the phase transformation from the orthorhombic to the fluorite lattice, x must have a value significantly larger than 0.6. However, for powder LSF, it was found that the δ decreased by 0.3 after reduction in 1 bar of H_2 at 873 K.[28] Hence, this would correspond to a stoichiometry of (La,Sr,Fe)$O_{1.25}$, with the oxygen coefficient still being significantly larger than 1 (no exact coefficients are given for the other elements as their exact ratios are not known due to the exsolution process removing Fe from the lattice). Consequently, the reduction in high vacuum, which is not as strongly reducing as hydrogen, may be expected to lead to lower oxygen deficiencies and, thus, to the formation of the fluorite phase and not the rock-salt phase. However, further studies are needed in order to confirm this. Also note that this analysis is based on the surface chemical states, as previously determined using XPS.[3] As mentioned in the introduction, this seemingly contradicts bulk data based on Moessbauer spectroscopy that reveal the presence of Fe(IV).[19,20] However, the consideration of this higher oxidation state only renders the oxygen deficiency values (δ, x) smaller, further substantiating the hypothesis that the transformation leads to the formation of the sub-stoichiometric fluorite phase.

In Fig. 2C, the position of the *Pmma* (031) or $Fm\bar{3}m$ (111) reflection is plotted as a function of the temperature. From 773 K to 823 K, the peak moves to a lower reciprocal distance, corresponding to an enlargement of the unit cell volume. This is the expected behavior due to thermal expansion. However, towards 873 K, the peak location increases again, implying a shrinking unit cell despite the higher temperature. Above 873 K, the expected behavior with a linear decrease of the peak position can be observed (the dashed lines serve as guides to the eye to illustrate this). The sudden change in peak position has previously been shown to be characteristic of phase transitions in various oxides.[3,21,55] In this case, the apparent shift in the unit cell dimensions also serves as a proof of the phase transformation in this temperature range, which is further corroborated by the drastically changing diffraction pattern.

Bright field TEM images of the thin films at 823 K and 1123 K are given in Fig. 3A and B, respectively. These exemplary images highlight the changes of the morphology the phase transformation and the sintering processes cause: while the contrast in panel A (corresponding to a temperature of 823 K, where the orthorhombic phase is present) does not reveal any clearly defined crystallites in the perovskite (and, in fact, is reminiscent of an amorphous material), there are a few grains featuring dark contrast, corresponding to already exsolved metallic Fe particles. At the higher temperature (panel B, $Fm\bar{3}m$ phase), however, the contrast of the oxide changes noticeably: the contrast is lighter and the different particles are more distinct. There also are some exsolved metal particles visible, with the larger ones featuring dark contrast at their edges (*e.g.* in the top right corner), which is assumed to be a type of Bragg contrast.

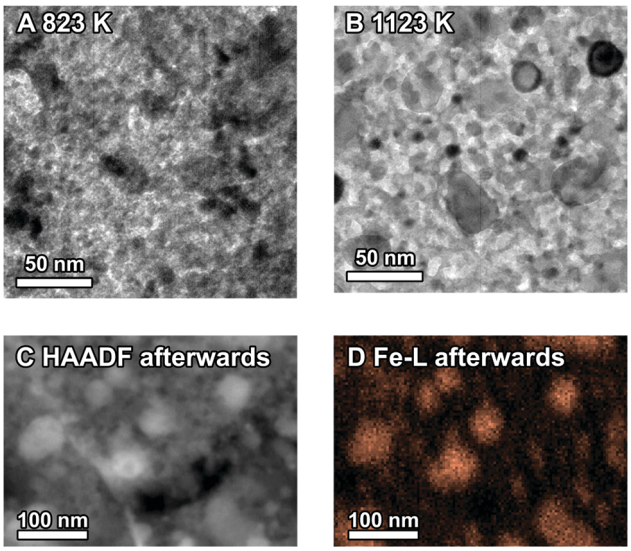

Fig. 3 Bright field images obtained at 823 K (A) and 1123 K (B), respectively, as well as an HAADF micrograph recorded after the heating experiment (C) and its corresponding Fe distribution as acquired using EDX (Fe-L line, panel D).

Interestingly, some of the Fe particles observed at 1123 K are smaller than those first found at 823 K, even though strong sintering phenomena are expected at the higher temperature. Nevertheless, this can be explained by a two-stage exsolution process where some particles are first exsolved from the orthorhombic phase at low temperatures, whereas the newly formed cubic phase requires a higher temperature for exsolution (see Fig. 4 below, which corroborates this theory).

After the *in situ* heating experiment, the specimen was cooled down to room temperature again and high angle annular dark field (HAADF) images, together with EDX spectrum images, were recorded. The HAADF micrograph is shown in Fig. 2C and the iron map (depicting the Fe L edge intensity) in panel D. The Fe particles can be clearly discerned by the bright contrast in the HAADF image, resulting both from a higher average mass than is the case for LSF and from a locally higher thickness due to the exsolved particles on the surface of the perovskite. The iron map in Fig. 2D confirms this assignment as the cumulations of Fe concentration coincide well with the bright contrast in the HAADF image.

The evolution of the exsolved iron particle size as a function of the temperature, based on the *in situ* experiments, is displayed in the upper panel of Fig. 4. The sizes were determined by measuring the diameters of more than 100 Fe particles at each temperature and fitting a Gauss function to the histogram in order to determine the most frequent size. The error bars shown in the graph represent the errors obtained by this fitting procedure. At 823 K, where the exsolution starts for the first time, the particles have a diameter of approximately 21 nm, which then increases to a plateau of just below 30 nm for the subsequent temperatures until 1023 K, above which the sizes increase again significantly. The particle density (lower panel) exhibits a correlating trend as the concentration of particles remains approximately constant up to 1023 K as well before increasing rapidly.

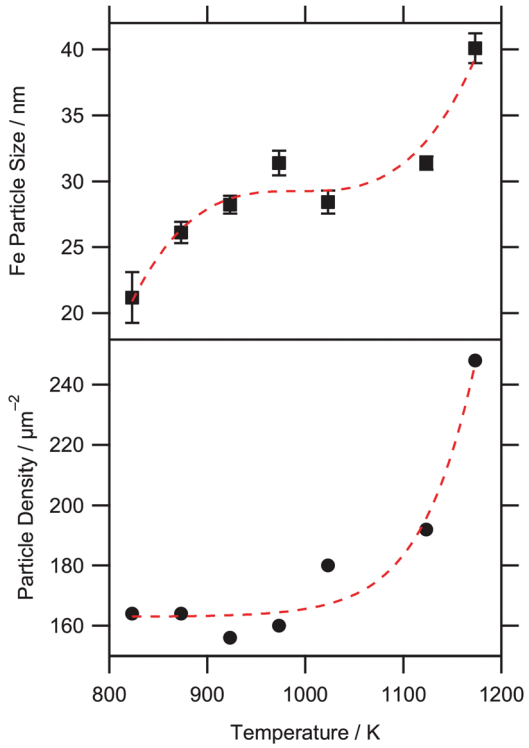

Fig. 4 Sizes of the exsolved Fe particles (top panels) and Fe particle densities, as measured using a 500 nm × 500 nm area (bottom panel).

This behavior can be explained by the orthorhombic-to-cubic phase transformation occurring between 823 K and 873 K: at 823 K, the exsolution already starts from the orthorhombic structure. Subsequently, the Fe particles sinter slightly, increasing their diameters. Any further formation of metallic iron, however, is then inhibited by the change in the crystal structure that occurs when going to 873 K, where the exsolution does not appear to be possible under these conditions. In fact, these data suggest that the iron exsolution from the transformed (possibly fluorite/rock-salt) LSF is shifted to higher temperatures as compared to the cubic perovskite, which was obtained by reduction of the powderous material in hydrogen at atmospheric pressures.[3] This could either result from the fact that the reduction here is performed in high vacuum as opposed to H_2, or it could be caused by the different crystal structures: whereas the powder in our previous work started out as a rhombohedral structure and the exsolution of iron particles only started after the phase transformation to the cubic perovskite structure,[3] in the thin films presented here, the exsolution from the lattice already happened before the transition to the cubic structure. Thus, the thin film in the $Fm\bar{3}m$ structure already has an iron deficiency when it is formed, which, in addition to a potentially different exsolution behavior of the $Fm\bar{3}m$ structure, might also inhibit any further formation of metallic Fe at these temperatures. Above 1123 K, however, this limitation is overcome and Fe segregates to the surface again.

3.2 Rhombohedral powderous LSF

LSF powder was further employed to investigate the oxidation states in its oxidized and reduced states more closely. In a

previous study, *ex situ* XPS data revealed the surface to contain Fe(III) and Fe(II).[3] This, however, was contradictory to magnetic studies that indicate the presence of an Fe(IV)/Fe(III) couple.[19,20] In order to ensure that the different oxidation states were not an artifact introduced by the *ex situ* measurements, we employed *in situ* core level spectroscopy (XPS and XANES). Furthermore, as these techniques yield information about the(sub-)surface, we also conducted *ex situ* neutron scattering of equivalently treated specimens to investigate the bulk oxidation states and the concentrations of oxygen vacancies. These questions will be addressed in the following subsections.

3.2.1 The surface redox chemistry of iron in reductive environments. Temperature-dependent near-ambient pressure X-ray absorption near-edge spectra (NAP-XANES) of the reduction of rhombohedral LSF powders at H_2 pressures of 0.3 hPa are presented in Fig. 5. Panels A and B show the Fe-L edge spectra acquired in total electron yield (TEY) and Auger electron yield (AEY) modes, respectively, with the latter being more surface-sensitive (TEY spectra also sample the outer sub-surface region), while, in C, Fe-L spectra calculated for different oxidation states (Fe(II), Fe(III) and Fe(IV), with initial/final states of $3d^6/2p^53d^7$, $3d^5/2p^53d^6$ and $3d^4/2p^53d^5$, respectively) using the multiplet ligand-field theory *via* the Xclaim code are shown.[56] Here, an octahedral crystal field, corresponding to the [FeO_6] coordination in the (cubic) perovskite structure is employed. Even though this polyhedron is slightly distorted in the rhombohedral structure, the influence of the distortion on the spectra is expected to be negligible, especially considering that the spectrum was

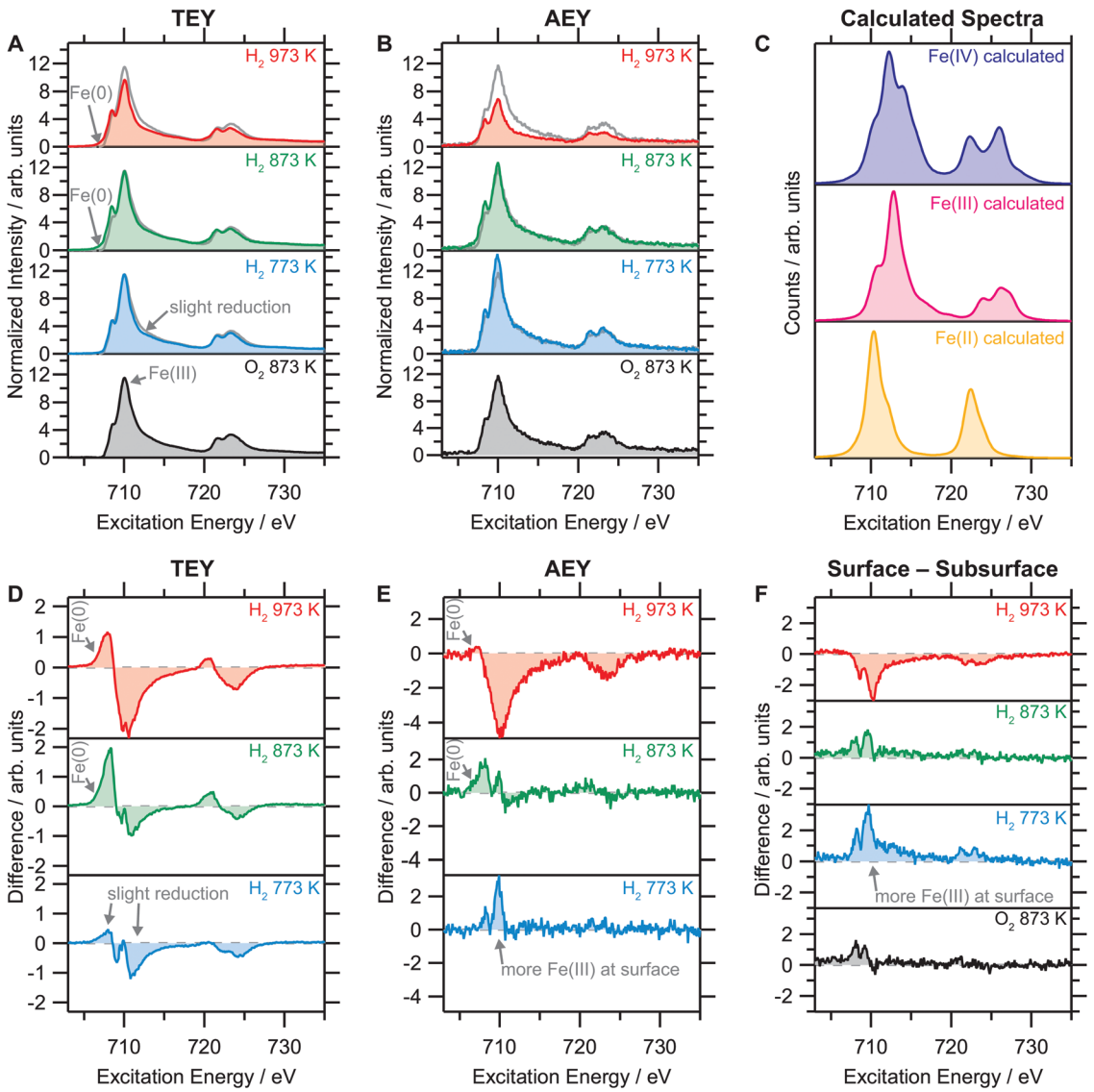

Fig. 5 Fe-$L_{2,3}$ edges obtained by temperature-programmed NAP-XANES upon reduction (all measurements were conducted in pressures of 0.3 hPa). (A) Total electron yield, (B) surface-sensitive Auger electron yield spectra. In (A) and (B), the respective spectra obtained for the pre-oxidation step are included in the other panels as a light grey curve to give the reader a visual reference of the spectral changes. In (C), calculated spectra for different iron oxidation states are displayed. (D and E) show the changes in the spectra relative to the oxidized sample for the TEY (D) and AEY (E), respectively. In (F), the differences between the AEY and TEY spectra are displayed, highlighting changes between the surface and surface-near regions.

broadened by Gauss and Lorentz functions with full widths at half maximum (FWHMs) of 1 eV. A crystal field separation of $10Dq$ = 2 eV was used (which is very close to literature values of perovskite ferrites[57]) and hybridization was neglected. These settings were used for all oxidation states to ensure comparability.

For a better visualization of the effect of the reduction, the spectra recorded during the pre-oxidation in 0.3 hPa O_2 at 873 K are superimposed on each spectrum as a grey line, and panels D and E show the TEY and AEY difference spectra, highlighting the spectral changes as compared to the O_2 873 K data.

In the pre-oxidized state, the TEY and AEY spectra look very similar (due to the larger number of detected particles, the signal-to-noise ratio in the TEY mode is better). In both cases, there is a distinct shoulder at the absorption edge. This is not an indication of an already reduced perovskite, but rather is an expected feature of octahedrally coordinated Fe(III) ions, as shown by the excellent agreement with the predicted Fe(III) spectrum in Fig. 5C. In contrast, the spectral shapes of the Fe(II) and Fe(IV) species do not match the observed recordings, which is especially noticeable in the L_2 edge. Hence, the perovskite in its fully oxidized initial state prior to the reduction can be considered to be in an Fe(III) state. By subtracting the TEY spectrum from the AEY one, the difference between surface and sub-surface can be obtained (panel F). The positive net differences at the excitation energies of the L_3 and L_2 edges in Fig. 5F reveal there to be a slight enrichment of Fe in the surface region compared to the area underneath it. The reduction of this sample in 0.3 hPa of pure hydrogen at 773 K leads to minor changes in the sub-surface-sensitive absorption spectra (A, D, colored blue): in both the L_3 and L_2 edges, the intensity after the maximum is slightly lower than in the oxidized case (grey curve), causing a more noticeable kink. This can be explained by the narrower peak shape of the Fe(II) species as compared to the Fe(III) ones. Additionally, the shoulder at the low-energy side of the absorption edge is more pronounced, with its maximum being clearly discernible. In AEY mode (B, E), the spectrum changes more noticeably due to the reduction, as the intensity of the Fe-L edge is increased in general, and also the shoulder at the edge is more pronounced than in TEY mode. These changes can be interpreted to stem from a slight reduction of the Fe species, which is accompanied by a segregation of these ions to the surface region (as proven by the AEY-TEY difference spectra in F, which feature a positive net signal).

When the reduction temperature is raised to 873 K, a shoulder appears at the low-energy side, both for the TEY and the AEY spectra, indicating the formation of metallic iron. The intensity of the main maximum is approximately the same as in the oxidized state, which means that the intensity is lowered at the surface. This can be explained by the exsolution of Fe(0) at the surface, thus blocking the perovskite signal at the sites of the particle formation from appearing in this surface-sensitive spectrum. This is further corroborated by the fact that the corresponding metallic Fe signal is stronger at the surface than in the sub-surface region. At 973 K, finally, the intensity of the iron edge in the AEY spectrum decreases significantly, as is also visible by the negative intensity in the top-most difference spectrum in panel E. The most probable explanation for this phenomenon is the sintering of the exsolved iron particles at this high temperature, reducing the amount of metallic iron at the surface in favor of the iron-depleted perovskite. In the TEY spectra, representing the sub-surface region, this effect is not as severe: the intensity of the Fe-L edge is only slightly lower than in the oxidized case. In fact, the negative intensities in panel F indicate that the surface now is depleted in iron (both metallic and oxidized) in contrast to the sub-surface region.

Thus, the XANES results show that the perovskite is first slightly reduced at a temperature of 773 K in 0.3 hPa of H_2, which is accompanied by an agglomeration of (reduced) Fe species at the surface. At 873 K, the iron exsolution starts at these conditions, as seen by a shoulder appearing at the onset of the absorption edge. The sintering of these iron particles at 973 K then causes a reduction in the general intensity of these (sub-)surface-sensitive spectra, and the LSF sample itself is depleted in Fe at the surface.

In order to get complementary information to the XANES data, NAP-XPS was carried out simultaneously under the same conditions as the X-ray absorption experiments. The results of these measurements are given in Fig. 6. The Fe $2p_{3/2}$ spectra in Fig. 6A were recorded at the same temperatures as the XANES results in Fig. 5. These spectra were fitted with reference spectra obtained for Fe_2O_3 and FeO (prepared *in situ* from iron(II)oxalate to prevent its decomposition by disproportionation) in order to determine the oxidation states, which is why only half of the doublet is shown.[3,28] A Gauss–Lorentz peak with additional asymmetry was used to represent metallic iron. After the pre-oxidation, only Fe(III) can be found in the spectrum (rendered in red). The slight reduction that was observed in the XANE spectra after the treatment in 0.3 hPa of H_2 at 773 K is visible here, too, in that there are approximately 6% of Fe(II) present. This low concentration of the reduced species is in contrast to previous *ex situ* measurements, where the reduction was carried out at atmospheric pressure, and where the perovskite was already found to become reduced above 673 K.[3] However, the shift to higher temperatures is a clear result of the significantly lower pressure.

The degree of reduction increases significantly at 873 K, where the spectrum is composed of 9% Fe(III), 89% Fe(II) and 2% Fe(0) (although the latter is already close to the standard error). The latter indicates that the exsolution starts at this temperature and, thus, is in excellent agreement with the XANES results. At the highest reduction temperature, 973 K, the perovskite is further reduced, with the Fe(III) content in the surveyed region now being below 2%, and also the metallic iron content increases to 4.3%.

At 973 K, time-resolved measurements were conducted. Some exemplary spectra are displayed in Fig. 6B. With increasing reduction time, the amount of Fe(0) increases. As seen from the upper panel in Fig. 6C, in which the metallic iron concentration is plotted as a function of the reduction time, the exsolution stagnates after about 2000 s as the concentration reaches a plateau. The evolution of the amount of exsolved iron can be fitted by an Avrami function (red curve),

$$c(\mathrm{Fe}^0) = c_0 + (c_{\max} - c_0)(1 - \exp(-k^n t^n)), \qquad (1)$$

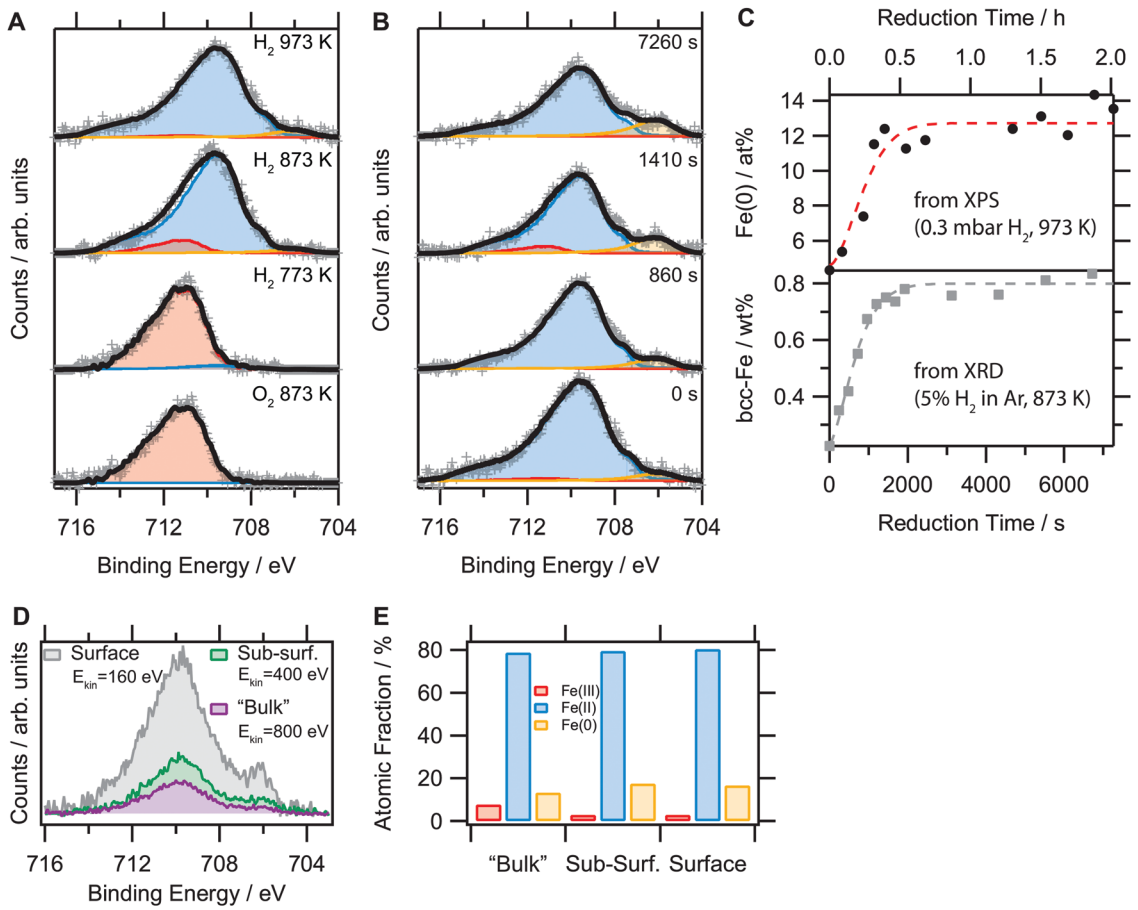

Fig. 6 NAP-XPS results for the powder system. (A) Fe $2p_{3/2}$ regions as a function of the reduction temperature. (B) Spectra resulting from a time-resolved experiment at 973 K and (C) an Avrami fit of the Fe(0) concentrations as a function of the time (upper panel), as well as the respective fit of the crystalline Fe concentration from previous XRD measurements (in 5% H_2/Ar at 873 K, lower panel),[3] included for comparison. (D) Shows a depth profile at 973 K and the resulting concentrations are given in (E). The depth profile was recorded with photon energies of 870 eV (surface-sensitive, $3\lambda \approx 1.8$ nm), 1110 eV (sub-surface $3\lambda \approx 3$ nm) and 1510 eV (labeled "bulk" to show that it penetrates the sample further than at 1110 eV, $3\lambda \approx 5$ nm).

yielding a rate constant, k, of 1×10^{-3} s^{-1} and an exponent, n, of 1.7. c_0 and c_{max} are the offset and scale of this function, respectively (required because, upon reaching the target temperature, there already is metallic iron present). The applicability of the Avrami equation indicates that this process is diffusion-limited, which was also found for the reduction at 1 bar.[3] An example of the Avrami fit of the iron concentration as obtained from Rietveld analysis of *in situ* XRD data from ref. 3 is displayed in the lower panel (the error bars that were included in the previous work were left out here to better demonstrate the similarities). Despite the higher partial pressure of H_2 during the XRD measurements (approximately 50 hPa) and the lower temperature (873 K *versus* 973 K), the agreement of both fits is excellent. While, based on the diffraction experiments alone, it was not clear whether this trend was actually the exsolution of iron or just the crystallization (with the exsolution happening quicker, but the resulting iron particles being amorphous and, thus, invisible to this technique), these similarities between the XPS and XRD data imply that it were in fact the exsolution kinetics that had been observed (*i.e.* the exsolved iron is crystalline from the start).

After the time-dependent experiment, a depth profile was created by varying the photon energy. This way, spectra with different degrees of surface-sensitivity were obtained, as drawn in Fig. 6D. These spectra were corrected for the different photon intensities as well as the different cross sections, *i.e.* the areas correlate directly to the concentrations. At the surface (light grey, the beam energy was 870 eV, resulting in an escape depth of $3\lambda_{IMFP} \approx 1.8$ nm according to the predictive G-1 formula),[58] the amount of metallic iron is the largest—and the intensity of the whole region is the largest as well. In the "bulk" ($h\nu$ = 1510 eV, corresponding to a kinetic energy of about 800 eV and an escape depth of $3\lambda_{IMFP} \approx 5$ nm), the intensity is the lowest due to the already-discussed surface segregation of the iron species. It is labeled "bulk" in the graphic to highlight its decreased surface-sensitivity compared to the other two spectra, even though it is not truly as bulk sensitive as the neutron diffraction data in the next sections (as it only samples the outermost 5 nm). The green spectrum (corresponding to a sub-surface sensitivity) was acquired with a photon energy of 1100 eV ($3\lambda_{IMFP} \approx 3$ nm). The relative concentrations of the different oxidation states are given in Fig. 6E.

3.2.2 The difference between bulk and surface oxidation states. NAP XPS and XANES revealed the surface, in its oxidized state, to contain only Fe(III). This, however, is in disagreement with published Moessbauer spectra, which suggest the presence of Fe(IV) at room temperature.[19,20]

In principle, it could be conceived that the Fe(IV) species are reduced due to the lower oxygen partial pressures in the XP spectrometers (operating in UHV conditions or at about 0.3 hPa for the NAP system). According to Kuhn *et al.*,[59] the oxygen deficiency, δ, is related to the partial pressure of O_2 *via*

$$p(O_2) = \frac{1\times10^3\,\text{hPa}}{16}\left[-\frac{1}{K_{Ox}{}^{1/2}}\frac{(2\delta-0.4)(3-\delta)^{1/2}}{(2\delta+0.6)\delta^{1/2}} + \left(\frac{1}{K_{Ox}}\frac{(2\delta-0.4)^2(3-\delta)}{(2\delta+0.6)^2\delta}+\frac{K_i}{K_{Ox}}\frac{4(3-\delta)(1.4-2\delta)}{(2\delta+0.6)\delta}\right)^{1/2}\right]^4. \quad (2)$$

δ is the oxygen deficiency in $La_{0.6}Sr_{0.4}FeO_{3-\delta}$, K_{Ox} and K_i are the equilibrium constants for te filling of oxygen vacancies and the disproportionation of Fe, respectively, as detailed by Kuhn *et al.*[59] This equation is plotted for two temperatures (873 K, as used in this work for the pre-oxidation in the NAP-XPS and XANES experiments, and 298 K, corresponding to the previous *ex situ* XPS measurements in ref. 3) in Fig. 7. The equilibrium constants were derived from the thermodynamic properties also given by Kuhn *et al.*[59] At a pressure of 0.3 hPa and a temperature of 873 K, δ is only 0.04 (see the dashed grey lines). However, in order to completely remove all Fe(IV) species upon reduction, δ would have to be 0.2 (corresponding to the horizontal plateaus in Fig. 7). In fact, for δ = 0.14, still 32% of all Fe species would be in the +4 oxidation state. This is further corroborated by the curve for room temperature (rendered in blue): there, the typical oxygen partial pressures in the UHV-based instrument of about 1×10^{-11} hPa cause no significant reduction of the iron ions at all. Hence, the same oxidation states in the bulk and at the surface would mean that Fe(IV) would have to be visible in all the spectra, which clearly is not the case. Thus, a reduction due to the vacuum can be excluded and the surface indeed exhibits different states than what was observed for the bulk using the Moessbauer spectra.

In order to investigate this discrepancy more closely, we conducted neutron scattering experiments, which yield information about the magnetic states of the specimens and, thus, about the oxidation states. The respective diffraction pattern of a fully oxidized specimen is given in Fig. 8. This sample has been calcined in air at 1173 K for 5 h, and XRD measurements, conducted at a synchrotron X-ray source, have shown it to be rhombohedral in structure (see the diffractograms in Fig. 9A and B).

The black curve in Fig. 8 denotes the calculated diffractogram from the Rietveld refinement, whereas the grey crosses mark the experimental data. Both are shown to coincide nicely, as affirmed by the difference between experimental and calculated intensities, represented by the light grey curve at the bottom of the panel. More details on this investigation are given in the next section.

Additionally, there is a peak at about 23° (labeled as 101*) that cannot be attributed to the nuclear (rhombohedral) structure, but rather stems from the antiferromagnetic coupling of Fe in this perovskite.[19] The varying intensity of this reflex for the three treatments (air, nitrogen and hydrogen/argon at the respective temperatures given in Fig. 8 and 9) implies a changing magnetic moment of iron and, hence, differences in the oxidation states. The magnetic moments were calculated by refining the diffraction data with the rhombohedral unit cell and a magnetic propagation vector k = (0,0,0). For this, the magnetic irreducible representations for Fe (at the 8b Wyckoff site) were determined by the BASIREPS software, consisting of two 1-dimensional and one 2-dimensional irreducible representations,

$$\Gamma_{Fe}^{8b} = 1\Gamma_2^{(1)} + 1\Gamma_4^{(1)} + 2\Gamma_5^{(2)}. \quad (3)$$

Only the magnetic structure corresponding to $1\Gamma_2^{(1)}$ resulted in adequate results when fitted to the experimental data (Fig. 8 and 9). This representation indicates an antiferromagnetic coupling of the Fe sites at (0,0,0) and (0,0,1/2) along the c axis,

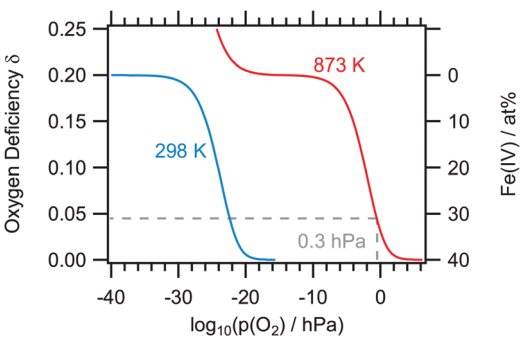

Fig. 7 The oxygen deficiency, δ (in $La_{0.6}Sr_{0.4}FeO_{3-\delta}$), as a function of the (logarithmic) oxygen partial pressure at temperatures of 873 K (red curve) and 298 K (blue), calculated according to Kuhn *et al.*[59] The right axis denotes the Fe(IV) concentration at each δ value for this compound (in atomic percent).

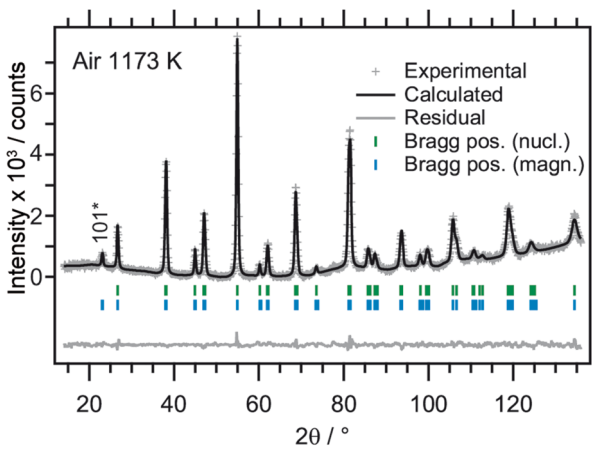

Fig. 8 Neutron diffraction data of an LSF sample that was calcined in air at 1173 K prior to the measurement (which was conducted at room temperature). The reflex marked with 101* stems from the antiferromagnetic ordering along the [001] direction.

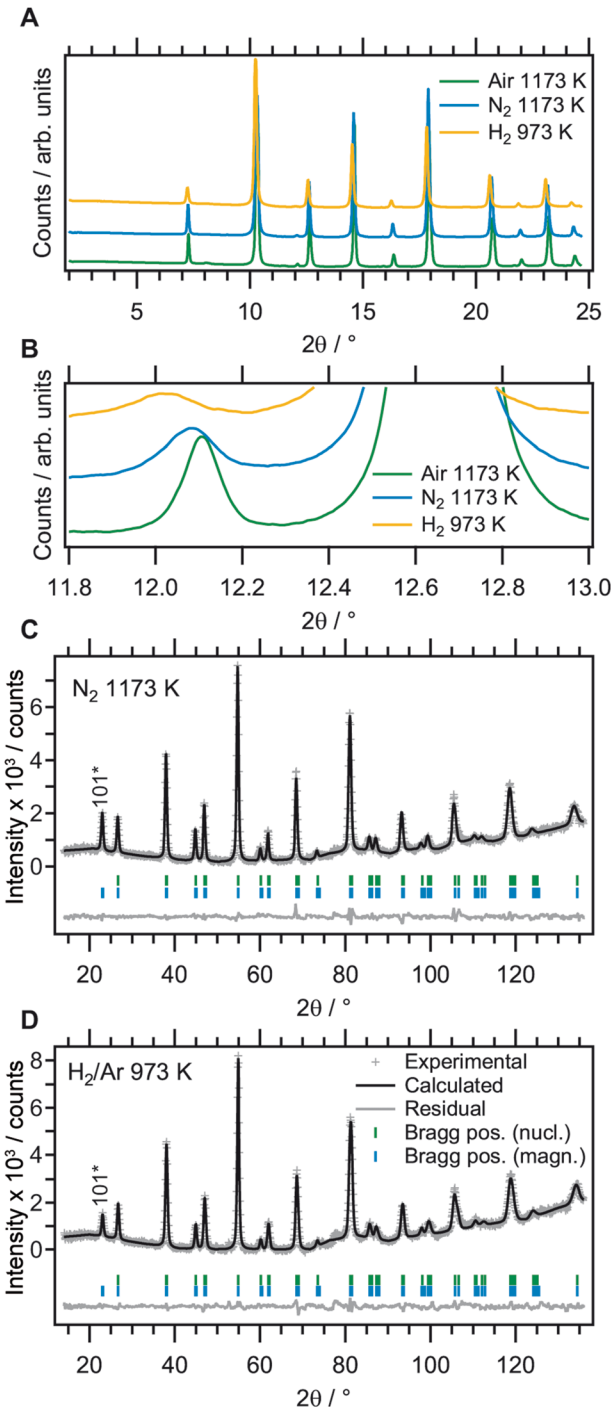

Fig. 9 (A) Synchrotron XRD patterns of the samples heated in air, nitrogen and hydrogen to 1173 K, 1173 K and 973 K, respectively. (B) Detailed view of the region around the rhombohedral (113) reflex, which is present in all specimens. The lower panels show the results of the structural refinement of neutron diffraction data of LSF heated in (C) N_2 to 1173 K and (D) H_2/Ar to 973 K.

which is in good agreement with literature data.[19] The resulting magnetic moments (as multiples of the Bohr magneton, μ_B) are listed in Table 2.

For the oxidized sample, the magnetic moment can be calculated to be 1.46(4) μ_B (μ_B being the Bohr magneton). This is in excellent

Table 2 Structural parameters from the refinement of the neutron diffraction data for LSF at 293 K in space group $R\bar{3}c$ (no. 167; Z = 6). H_2/Ar is the mixture of 5% of H_2 in argon

		Air	N_2	H_2/Ar
Atoms/Pos.	Parameters	1173 K	1173 K	973 K
Fe1	B_{iso}/Å$^{2\,b}$	0.77(4)	0.596(4)	0.62(5)
6b	μ_B[c]	1.46(4)	2.74(3)	3.51(3)
(0,0,0)[a]				
(La/Sr)1	B_{iso}/Å^2	1.19(4)	1.18(5)	1.34(9)
6a	occ. (La/Sr)[d]	0.6/0.4	0.6/0.4	0.6/0.4
(0,0,0.25)				
O1	x	0.4571(3)	0.4651(3)	0.4628(7)
18e	B_{iso}/Å^2	1.61(6)	2.39(8)	2.68(9)
(x,0,0.25)	occ.	0.990(4)	0.976(6)	0.934(6)
Lattice	a/Å^2	5.5278(2)	5.5369(2)	5.5469(3)
Parameters	c/Å^2	13.4545(6)	13.5187(9)	13.555(2)
Cell volume	V/Å^3	356.04(2)	358.92(3)	361.19(5)
Discrepancy	R_p	2.3	2.2	1.7
factors/%	R_{wp}	2.9	2.9	2.2
	R_{exp}	2.3	2.1	1.6
	X^2	1.5	1.9	1.9

[a] Notes: Wyckoff positions (fractional atomic coordinates). [b] Isotropic temperature factors. [c] Magnetic moment. [d] Occupation factor.

agreement with literature data of Fe(IV)-containing compounds.[16–18] Furthermore, the oxygen occupational factor was determined as 0.990(4), *i.e.* there are only negligible amounts of vacancies. Hence, this refinement clearly states the presence of Fe(IV), while, with XANES and XPS, only Fe(III) was found in the fully oxidized state. While this appears contradictory, it has to be taken into account that these techniques do not sample the same regions of the specimen: to XANES and XPS, only the (sub-)surface areas are accessible, whereas neutron diffraction is a bulk-sensitive method. This difference in oxidation states suggests a completely different chemistry at the surface and in the bulk: the X-ray spectroscopy results would imply that the surface compensates for the substitution of La^{3+} by Sr^{2+} by the introduction of oxygen vacancies, thus preserving the Fe(III) states. According to neutron diffraction results, on the other hand, the bulk accounts for the substitution by a (partial) increase of the Fe oxidation state to Fe(IV).

A possible reason for this disparity between bulk and surface could be the instability of the Fe(IV) states at the surface, which might lead to an electronic rearrangement. Alternatively, the perovskite potentially adopts a slightly different structure close to the terminating surface, which could cause a decrease of the coordination number of Fe and, consequently, its oxidation state.

3.2.3 Oxygen vacancies and magnetic properties of untransformed rhombohedral LSF under reducing conditions. According to synchrotron-based *in situ* XRD studies,[3] the initially rhombohedral ($R\bar{3}c$) LSF undergoes a phase transformation to the cubic polymorph ($Pm\bar{3}m$) in the presence of low oxygen partial pressures. However, this perovskite is a solid oxide fuel cell anode candidate (*i.e.* it is exposed to strongly reductive gases) and, there, this transformation is undesired as it would cause cracking and the subsequent failure of the cells.

As there were indications of the cubic structure being metastable (and only stabilized by oxygen vacancies), we increased heating rate, target temperature and dwell time at the highest temperature (see the experimental section for details) to retain the rhombohedral structure, and conducted synchrotron-based XRD and neutron measurements. This combination is required because the differences in the diffractograms between the two structures are very small. Fig. 9 shows the results of these crystallographic measurements. In panel A, the X-ray diffractograms of LSF species calcined in air at 1173 K, in nitrogen (1173 K) and in a mixture of 5% hydrogen in argon (973 K) are given. Fig. 9 displays a magnified region between $2\theta = 11.8^\circ$ and 13.0°, which contains the (113) reflex of the rhombohedral phase (at about 12.1°), but no signal from the cubic perovskite.[3] All three samples exhibit this peak, proving that all three are indeed rhombohedral, even the ones heated in N_2 and H_2/Ar. Thus, the transition to the cubic phase could successfully be inhibited, which would be a promising result regarding the application in SOFCs. However, further *in situ* studies are required to ascertain whether the transition does not occur at all in these conditions or whether the temporarily formed cubic perovskite simply transforms back again at these high temperatures.

However, these X-ray diffractograms do not permit the refinement of the oxygen site occupancies. Therefore, high resolution neutron diffraction measurements were conducted. Based on the XRD results, the rhombohedral structure ($R\bar{3}c$) was used as the foundation of the Rietveld analyses of the neutron diffractograms in Fig. 9C and D. The recorded data (and those shown before in Fig. 8) can be fitted well with this structure (see the negligibly small residual signal and the low discrepancy factors in Table 2).

As already discussed, the oxidized sample features a magnetic moment of 1.46(4) μ_B, indicating the presence of Fe(III) and Fe(IV).[16–18] When the sample is heated to 1173 K in nitrogen, this value increases to 2.74(3) μ_B, and it is highest when reduced in 5% H_2 in Ar at 973 K, at 3.51(3) μ_B This is in line with an increasing Fe(III) concentration as the magnetic moment for $LaFeO_3$, in which the iron is present solely as Fe(III), is 4.6(2) μ_B.[60] It is also plausible that the magnetic moment – and, thus, also the amount of Fe(III) – is highest when the sample is exposed to a hydrogen/argon mixture, the reductive potential of which is higher than that of inert nitrogen.

In addition to the magnetic moments, conclusions about the degree of reduction can be drawn based on the oxygen site occupation factors that are also given in Table 2. After calcination in air, it is 0.990(4), *i.e.* the sample can be considered to be fully oxidized with no vacancies. However, as it is heat-treated in nitrogen (1173 K), this is lowered to 0.976(6). After reduction in hydrogen, the vacancy concentration is significantly larger as the occupancy of O is 0.934(6). When these occupation factors are transformed to oxygen deficiencies, δ in $La_{0.6}Sr_{0.4}FeO_{3-\delta}$, values of $\delta = 0.072(18)$ for the annealing in nitrogen and $\delta = 0.198(18)$ in the hydrogen/argon mixture (5%) are obtained. This is also in line with the unit cell volume (see Table 2), which is smallest for the oxidized sample (356.04(2) Å^3) and increases for the powder treated in nitrogen (358.92(3) Å^3). At 361.19(5) Å^3, however, the unit cell volume is largest after reduction in the H_2/Ar mixture. This can be explained by the larger ionic radius of Fe(III) as compared to Fe(IV).

The fact that the neutron data imply an Fe(IV) → Fe(III) transition upon reduction (both derived from the magnetic moments and the O site occupancies), whereas the XP spectra clearly can be fitted by a linear combination of Fe(III) and Fe(II) reference spectra appears to be contradictory. However, again the different sampling areas of both techniques have to be taken into account: while XPS and AEY/TEY XANES are surface-sensitive, neutron diffraction is a bulk-sampling method. Thus, these results imply that the chemistry at the surface and in the bulk is drastically different, both upon oxidation, as well as in reducing conditions. The surface was shown to transition from an Fe(III) termination to a reduced state, predominantly containing Fe(II), prior to the exsolution of Fe(0). This was both found in this work using *in situ* spectroscopy (with pressures in the 0.3 hPa range), as well as in a previous work with *ex situ* XPS (and reductions at atmospheric pressure).[3] In the bulk, however, significant amounts of Fe(IV) – induced by the substitution of La(III) with Sr(II) – are found. Moreover, this altered behavior is no artifact stemming from the untransformed reduced perovskite since the oxidized LSF is rhombohedral in any case and the prevented phase transformation only affects the samples treated in nitrogen or air.

4 Conclusion

We have demonstrated that the iron exsolution from lanthanum strontium ferrite perovskites under reductive conditions is not limited to the rhombohedral starting structure ($R\bar{3}c$), but also occurs when an orthorhombic phase is employed (*Pmma*). While, in the rhombohedral system, the exsolution is preceded by a phase transformation to the cubic $CaTiO_3$ type ($Pm\bar{3}m$), metallic Fe particles are already formed before any phase transformation in the orthorhombic structure takes place. In fact, after the onset of the exsolution process, the orthorhombic LSF thin films transform into an $Fm\bar{3}m$ structure, which most likely corresponds to the fluorite type. This transformation seems to stagnate the exsolution process, as determined from particle size distribution and densities (during *in situ* heating experiments in the TEM). Consequently, larger temperatures are required in order to induce the segregation of Fe(0) again from the new phase. This suggests that, in the orthorhombic case, a relatively small amount of oxygen vacancies is sufficient to trigger the exsolution, whereas, in the fluorite lattice, a larger amount (formed at higher reduction temperatures) is required.

Additionally, the oxidation states and oxygen vacancies of powderous rhombohedral LSF species were investigated with *in situ* X-ray photoelectron and absorption spectroscopy (XPS, XAS), as well as *via* neutron scattering. It could be determined that the oxidation states of iron at the surface are different than in the bulk. While the latter contains Fe(III) and Fe(IV), the surface does not exhibit any tetravalent iron species, but rather purely Fe(III), which subsequently is reduced to Fe(II) prior to the exsolution of metallic particles. The cause of this could be a

rearrangement process of the surface-near region, leading to a slightly different structure than in the bulk, which potentially is caused by a possible thermodynamic instability of Fe(IV) at the surface. It is, however, also conceivable that a different coordination environment at the surface induces the lowered oxidation state.

In order to unambiguously answer this question, additional advanced techniques such as aberration-corrected TEM are required, which has the capability of resolving the atomic structure directly. In addition, extended X-ray absorption fine structure (EXAFS) measurements in the surface-sensitive AEY mode in comparison to spectra acquired in the extremely bulk-sensitive fluorescence yield mode (where photons are detected instead of electrons, as was done in this work) potentially help to explain this phenomenon: by recording the spectral range far beyond the absorption edges, the pair distribution function around the respective atom can be derived, providing data about bond lengths and strengths. By analyzing this information gathered with surface and bulk sensitivity, structural differences in both regions are discernible.

Using near-ambient pressure XPS, we have also determined the kinetics of the iron exsolution (based on the emergence of the metallic component in the Fe 2p region), which are in excellent agreement with data from Rietveld analyses (which were based on the visible metallic iron reflexes).[3] Thus, it can be concluded that the exsolution and crystallization processes are strongly interlinked and occur simultaneously (instead of the iron being segregated in an amorphous state before crystallizing at higher temperatures). Furthermore, NAP XANES revealed the chemical differences of the surface and the sub-surface during the reduction in hydrogen.

Conflicts of interest

There are no conflicts of interest to declare.

Acknowledgements

This work was funded by the Austrian Science Fund (FWF) *via* grant F4503-N16. It was furthermore performed within the frameworks of the research platform ''Materials- and Nanoscience'' and the special PhD program ''Reactivity and Catalysis'' at the University of Innsbruck. The research leading to this result has been supported by the project CALIPSOplus under the Grant Agreement 730872 from the EU Framework Programme for Research and Innovation HORIZON 2020. X-ray spectroscopy was conducted at the ISISS-PGM beamline at BESSY II under the proposal number 17205597-ST. L. Schlicker appreciates the ALS for supporting his work with a doctoral fellowship. This work is part of the Cluster of Excellence ''Unifying Concepts in Catalysis'' coordinated by the Technische Universität Berlin. Financial support by the Deutsche Forschungsgemeinschaft (DFG) within the framework of the German Initiative for Excellence is gratefully acknowledged. The authors further thank the Advanced Light Source (which is supported by the Director, Office of Science, Office of Basic Energy Sciences, of the U.S. Department of Energy under Contract No. DE-AC02-05CH11231), where *in situ* XRD measurements were conducted at beamline 12.2.2 in the framework of AP program ALS-08865. We thank HZB for the allocation of neutron radiation beamtime within proposal 172-05912 ST.

References

1 D. Neagu, G. Tsekouras, D. N. Miller, H. Ménard and J. T. S. Irvine, *Nat. Chem.*, 2013, **5**, 916–923.
2 R. Thalinger, M. Gocyla, M. Heggen, B. Klötzer and S. Penner, *J. Phys. Chem. C*, 2015, **119**, 22050–22056.
3 T. Götsch, L. Schlicker, M. F. Bekheet, A. Doran, M. Grünbacher, C. Praty, M. Tada, H. Matsui, N. Ishiguro, A. Gurlo, B. Klötzer and S. Penner, *RSC Adv.*, 2018, **8**, 3120–3131.
4 A. K. Opitz, A. Nenning, C. Rameshan, R. Rameshan, R. Blume, M. Hävecker, A. Knop-Gericke, G. Rupprechter, J. Fleig and B. Klötzer, *Angew. Chem.*, 2015, **127**, 2666–2670.
5 T. Götsch, C. Praty, M. Grünbacher, L. Schlicker, M. F. Bekheet, A. Doran, A. Gurlo, M. Tada, H. Matsui, N. Ishiguro, B. Kloetzer and S. Penner, *ECS Trans.*, 2017, **78**, 1327–1341.
6 J. M. Haag, S. A. Barnett, J. W. Richardson and K. R. Poeppelmeier, *Chem. Mater.*, 2010, **22**, 3283–3289.
7 T. S. Oh, R. J. Gorte and J. M. Vohs, *NAM-24, Extended Abstract*, 2015, O-Tu-403-12.
8 C. Yang, J. Li, Y. Lin, J. Liu, F. Chen and M. Liu, *Nano Energy*, 2015, **11**, 704–710.
9 Y.-F. Sun, Y.-Q. Zhang, J. Chen, J.-H. Li, Y.-T. Zhu, Y.-M. Zeng, B. S. Amirkhiz, J. Li, B. Hua and J.-L. Luo, *Nano Lett.*, 2016, **16**, 5303–5309.
10 S. Simner, *Solid State Ionics*, 2003, **161**, 11–18.
11 A. Fossdal, M. Menon, I. Waernhus, K. Wiik, M.-A. Einarsrud and T. Grande, *J. Am. Ceram. Soc.*, 2004, **87**, 1952–1958.
12 S. E. Dann, D. B. Currie, M. T. Weller, M. F. Thomas and A. D. Al-Rawwas, *J. Solid State Chem.*, 1994, **109**, 134–144.
13 V. G. Sathe, S. K. Paranjpe, V. Siruguri and A. V. Pimpale, *J. Phys.: Condens. Matter*, 1998, **10**, 4045–4055.
14 T. Götsch, E.-M. Wernig, B. Klötzer, T. Schachinger, J. Kunze-Liebhäuser and S. Penner, *Rev. Sci. Instrum.*, 2018, 009902RSI.
15 G. Rupprechter, K. Hayek, L. Rendón and M. José-Yacamán, *Thin Solid Films*, 1995, **260**, 148–155.
16 Z. Chu, W. B. Yelon, J. B. Yang, W. J. James, H. A. Anderson, Y. Xie and S. K. Malik, *J. Appl. Phys.*, 2002, **91**, 7938.
17 J. B. Yang, Q. Cai, H. L. Du, X. D. Zhou, W. B. Yelon and W. J. James, in *Neutron Diffraction*, ed. I. Khidirov, InTech, 2012, ch. 5, pp. 101–116.
18 H. Oda, Y. Yamaguchi, H. Takei and H. Watanabe, *J. Phys. Colloques*, 1977, **38**, C1-121–C1-123.
19 J. B. Yang, W. B. Yelon, W. J. James, Z. Chu, M. Kornecki, Y. X. Xie, X. D. Zhou, H. U. Anderson, A. G. Joshi and S. K. Malik, *Phys. Rev. B: Condens. Matter Mater. Phys.*, 2002, **66**, 184415.
20 S. Sabyasachi, M. Patra, S. Majumdar, S. Giri, S. Das, V. S. Amaral, O. Iglesias, W. Borghols and T. Chatterji, *Phys. Rev. B: Condens. Matter Mater. Phys.*, 2012, **86**, 2761.

21 T. Götsch, W. Wallisch, M. Stöger-Pollach, B. Klötzer and S. Penner, *AIP Adv.*, 2016, **6**, 25119.
22 T. Götsch, B. Neumann, B. Klötzer and S. Penner, *Surf. Sci.*, 2019, **680**, 52–60.
23 L. Mayr, N. Köpfle, A. Auer, B. Klötzer and S. Penner, *Rev. Sci. Instrum.*, 2013, **84**, 94103.
24 H. Bluhm, M. Hävecker, A. Knop-Gericke, M. Kiskinova, R. Schlögl and M. Salmeron, *MRS Bull.*, 2007, **32**, 1022–1030.
25 D. F. Ogletree, H. Bluhm, G. Lebedev, C. S. Fadley, Z. Hussain and M. Salmeron, *Rev. Sci. Instrum.*, 2002, **73**, 3872–3877.
26 J. J. Yeh and I. Lindau, *At. Data Nucl. Data Tables*, 1985, **32**, 1–155.
27 J.-J. Yeh, *Atomic calculation of photoionization cross-sections and asymmetry parameters*, Gordon & Breach Science Publ. and AT&T Bell Laboratories, Langhorne Pa. and Yverdon [etc.] and Murray Hill N.J., 1993.
28 R. Thalinger, T. Götsch, C. Zhuo, W. Hetaba, W. Wallisch, M. Stöger-Pollach, D. Schmidmair, B. Klötzer and S. Penner, *ChemCatChem*, 2016, **8**, 2057–2067.
29 Helmholtz-Zentrum Berlin für Materialien und Energie, *JLSRF*, 2017, 3, A103.
30 J. Rodríguez-Carvajal, *IUCr Newsl.*, 2001, **26**, 12–19.
31 L. W. Finger, D. E. Cox and A. P. Jephcoat, *J. Appl. Crystallogr.*, 1994, **27**, 892–900.
32 J. Rodríguez-Carvajal, *Phys. B*, 1993, **192**, 55–69.
33 A. Doran, L. Schlicker, C. M. Beavers, S. Bhat, M. F. Bekheet and A. Gurlo, *Rev. Sci. Instrum.*, 2017, **88**, 13903.
34 L. Schlicker, A. Doran, P. Schneppmüller, M. Czasny, S. Penner and A. Gurlo, *Rev. Sci. Instrum.*, 2018, **89**, 33904.
35 T. Götsch, D. Hauser, N. Köpfle, J. Bernardi, B. Klötzer and S. Penner, *Appl. Surf. Sci.*, 2018, **452**, 190–200.
36 P. D. Battle, T. C. Gibb and P. Lightfoot, *J. Solid State Chem.*, 1990, **84**, 237–244.
37 C. Gammer, C. Mangler, C. Rentenberger and H. P. Karnthaler, *Scr. Mater.*, 2010, **63**, 312–315.
38 Z. S. Basinski, W. Hume-Rothery and A. L. Sutton, *Proc. R. Soc. London, Ser. A*, 1955, **229**, 459–467.
39 S. V. Náray-Szabó, *Naturwissenschaften*, 1943, **31**, 466.
40 W. C. Koehler and E. O. Wollan, *J. Phys. Chem. Solids*, 1957, **2**, 100–106.
41 W. Chérif, M. Ellouze, A.-F. Lehlooh, S. H. Mahmood and F. Elhalouani, *Hyperfine Interact.*, 2012, **211**, 153–164.
42 J. Y. Lee, J. S. Swinnea, H. Steinfink, W. M. Reiff, S. Pei and J. D. Jorgensen, *J. Solid State Chem.*, 1993, **103**, 1–15.
43 M. Vučinić-Vasić, B. Antic, A. Kremenović, A. S. Nikolic, J. Blanusa, S. Rakić, V. Spasojevic and A. Kapor, *J. Alloys Compd.*, 2007, **428**, 322–326.
44 P. Bouvier, E. Djurado, G. Lucazeau and T. Le Bihan, *Phys. Rev. B: Condens. Matter Mater. Phys.*, 2000, **62**, 8731–8737.
45 E. Kümmerle and G. Heger, *J. Solid State Chem.*, 1999, **147**, 485–500.
46 P. Aldebert and J. P. Traverse, *Mater. Res. Bull.*, 1979, **14**, 303–323.
47 R. L. Blake, R. E. Hessevick, T. Zoltai and L. W. Finger, *Am. Mineral.*, 1966, **51**, 123–129.
48 H. Okudera, K. Kihara and T. Matsumoto, *Acta Crystallogr., Sect. B: Struct. Sci.*, 1996, **52**, 450–457.
49 M. C. Verbraeken, E. Suard and J. T. S. Irvine, *J. Mater. Chem.*, 2009, **19**, 2766.
50 R. W. G. Wyckoff and E. D. Crittenden, *Z. Kristallogr. - Cryst. Mater.*, 1926, **63**, 144–147.
51 A. Altomare, C. Cuocci, C. Giacovazzo, A. Moliterni, R. Rizzi, N. Corriero and A. Falcicchio, *J. Appl. Crystallogr.*, 2013, **46**, 1231–1235.
52 M. Souadkia, B. Bennecer and F. Kalarasse, *J. Phys. Chem. Solids*, 2012, **73**, 129–135.
53 R. E. Carter, *J. Am. Ceram. Soc.*, 1959, **42**, 324–327.
54 P. A. Midgley and A. S. Eggeman, *IUCrJ*, 2015, **2**, 126–136.
55 T. Götsch, K. Ploner, J. Bernardi, L. Schlicker, A. Gili, A. Doran, A. Gurlo and S. Penner, *J. Solid State Chem.*, 2018, **265**, 176–183.
56 J. Fernández-Rodríguez, B. Toby and M. van Veenendaal, *J. Electron Spectrosc. Relat. Phenom.*, 2015, **202**, 81–88.
57 G. V. S. Rao, C. N. R. Rao and J. R. Ferraro, *Appl. Spectrosc.*, 2016, **24**, 436–445.
58 W. H. Gries, *Surf. Interface Anal.*, 1996, **24**, 38–50.
59 M. Kuhn, S. Hashimoto, K. Sato, K. Yashiro and J. Mizusaki, *Solid State Ionics*, 2011, **195**, 7–15.
60 S. A. Ivanov, R. Tellgren, F. Porcher, T. Ericsson, A. Mosunov, P. Beran, S. K. Korchagina, P. A. Kumar, R. Mathieu and P. Nordblad, *Mater. Res. Bull.*, 2012, **47**, 3253–3268.